Journal of Power Sources 327 (2016) 414–422

Contents lists available at ScienceDirect

Journal of Power Sources

journal homepage: www.elsevier.com/locate/jpowsour

Sinusoidal current and stress evolutions in lithium-ion batteries

Xiao-Guang Yang [a], Christoph Bauer [b], Chao-Yang Wang [a, *]

[a] *Department of Mechanical and Nuclear Engineering and Electrochemical Engine Center (ECEC), The Pennsylvania State University, University Park, PA 16802, USA*
[b] *BMW Group, Munich, Germany*

HIGHLIGHTS

- Diffusion induced stress in Li-ion battery anode is numerically modeled.
- Local stress and current evolve like sinusoidal waves in discharge process.
- The sinusoidal stress evolution is attributed to the staging behavior of graphite.
- Effects of DoD, C-rate and electrode thickness on stress evolution are studied.

ARTICLE INFO

Article history:
Received 8 June 2016
Received in revised form
29 June 2016
Accepted 20 July 2016

Keywords:
Lithium-ion battery
Mechanical degradation
Diffusion-induced stress

ABSTRACT

Mechanical breakdown of graphite materials due to diffusion-induced stress (DIS) is a key aging mechanism of lithium-ion batteries. In this work, electrochemical-thermal coupled model along with a DIS model is developed to study the DIS distribution across the anode thickness. Special attention is paid to the evolution behavior of surface tangential stress (STS) in the discharge process for graphite at different locations of the anode. For the first time, we report that the evolution of STS, as well as local current, at all locations of the anode, evolve like sinusoidal waves in the discharge process with several crests and troughs. The staging behavior of graphite active material, in particular the sharp change of open-circuit potential (OCP) of graphite in the region between two plateaus, is found to be the root cause for the sinusoidal patterns of current and stress evolution. Furthermore, the effects of various parameters, such as starting state of charge, discharge C-rate and electrode thickness on the current and stress evolutions are investigated.

1. Introduction

The last decade has witnessed an unprecedented research emphasis on lithium-ion batteries (LIBs) for applications in electric vehicles (EVs). The widespread penetration of EVs into the market requires the LIBs to be of high performance, safety and durability. When expecting EV lifetime of 10–15 years or more, the durability of LIBs becomes the bottleneck [1,2]. To this end, tremendous research efforts have been devoted to understanding the aging mechanisms of LIBs in order to improve their lifetime [3–5].

Mechanical breakdown of electrode materials due to diffusion-induced stress (DIS) is one of the key factors limiting the durability of LIBs [6–8]. Lithium insertion into or extraction from the lattice of electrode active material particles (EAMPs) induces volume expansion or contraction, resulting in mechanical stress that can potentially lead to fracture and decrepitation of EAMPs. For instance, graphite, the anode material used in almost all state-of-the-art LIBs, undergoes ~10% volume change in charge/discharge cycles. Silicon, a promising anode material in the future, undergoes volume change as high as ~400%. Kostecki and McLarnon [9] conducted a microprobe study on the structural stability of graphite in charge/discharge cycles, and observed significant structure damage of graphite after cycling. The fractured graphite can expose new surfaces to the electrolyte on which solid-electrolyte-interphase (SEI) forms, resulting in loss of cyclable lithium. Part of the graphite can even be lost (isolated from the main electron-conducting matrix) as a result of crack propagation, leading to both impedance growth and capacity decay. This kind of mechanical degradation can be much more serious if silicon is used as the anode material.

Mathematical models have been developed in the recent

---

* Corresponding author.
E-mail address: cxw31@psu.edu (C.-Y. Wang).

http://dx.doi.org/10.1016/j.jpowsour.2016.07.070

literature to predict the DIS in the intercalation and/or deintercalation process of EAMPs. Christensen et al. [10,11] developed an integrated model based on the theories of transport and elasticity to predict the stress in lithium manganese oxide (LMO) [10] and graphite particles [11]. They reported that the maximum stress increases with the C-rate and particle size. Similar results were also reported by Zhang et al. [12] in which they proposed a model based on the analogy between DIS and thermal stress, and applied it to predict the DIS in LMO particles. They also studied the DIS and heat generation in the process of linear sweep voltammetry of a single LMO particle [13]. Later on, Cheng and Verbrugge [14] simplified Zhang's approach by neglecting the stress-driven diffusion, and obtained analytical solutions for the evolution of stress and strain energy in a spherically shaped particle under either galvanostatic or potentiostatic operation. The predicted stress and strain energy then serve as criteria to assess the potential for crack nucleation [15] and to help identify battery operating conditions that are able to keep the mechanical stress below acceptable values [16]. A brief review and comparison of the above stress models was recently presented by Suthar et al. [17]. They also proposed using the maximum stress as criteria for developing optimal charging strategies. All the above studies contribute substantially to the understanding of the mechanical aging related to the DIS. Nevertheless, all of them focus only on a single electrode particle. The porous nature of the electrode, e.g. the variation across the electrode thickness, is neglected.

The experimental work of Kostecki and McLarnon [9] demonstrated that graphite particles close to the separator suffered from severe damage after cycling, whereas those close to the copper foil remained almost unchanged, indicating that the DIS is highly non-uniform across the electrode thickness. Garcia et al. [18] were among the first to consider the porous nature of the electrode in simulating the mechanical stress. They presented a two-dimensional model with spherical particles distributed within the electrode to predict the performance of the battery and the stress distribution. This model is useful in simulating performance of electrodes with complex microstructures, but is computationally rather expensive. A more practical approach is to combine the aforementioned single-particle DIS models with the macroscopic LIB models based on porous electrode theory [19,20]. Christensen [21] incorporated his previous single-particle stress model [11] into the macroscopic model of Doyle et al. [19], and analyzed the porous electrode effects on stress generation. The model predicts higher stress near the electrode/separator interface, and the peak stress increases with the increase of electrode thickness. Another type of model is proposed by Golmon et al. [22] and by Renganathan et al. [23], which combined the mechanical model of Zhang et al. [12] with the model of Doyle et al. [19]. They reported non-uniform stress distribution across the electrode thickness which is ascribed to the non-uniform current distribution. Local current is highest near the separator due to the shortest ionic transfer path (lowest ionic resistance), which induces highest DIS therein. Similar models are also adopted by Dai et al. [24], Takahashi and Srinivasan [25], and Suthar et al. [26], in which the effects of various operating conditions such as C-rate, electrode properties such as thickness, porosity and tortuosity, and EAMP properties such as particle diameter and Li solid-phase diffusivity, on the magnitude and distribution of DIS are investigated in detail. Nevertheless, most of these studies focus on the stress distribution across the electrode at only selected time instances. There is still, to the best of our knowledge, no systematic investigation on the evolution of stress in the entire discharge process for EAMPs at different positions of the electrode.

In this work, by incorporating the single-particle DIS model into our previous electrochemical-thermal (ECT) LIB model [27,28], we focused on the evolution of DIS of graphite at different positions of the anode during the galvanostatic discharge process. For the first time, we report that the DIS and local current of graphite anode evolve like decaying sinusoidal waves with several crests and troughs in the discharge process. These sinusoidal evolutions are found to be related to the staging behavior of graphite. Furthermore, the effects of various parameters, such as starting state of charge (SOC), C-rate, and electrode thickness on the current and stress evolutions are investigated.

2. Model description

2.1. Electrochemical-thermal coupled model

The presented model is based on our previous ECT model with the incorporation of the single-particle DIS model. The ECT model has been adopted extensively in the literature and demonstrated to be powerful in predicting the LIB performance at various kinds of electrochemical and thermal conditions [29–31]. The simulation domain is subdivided into solid- and electrolyte-phase, denoted by subscripts s and e and treated as superimposed continua with each phase having its own volume fraction and without considering the detailed microstructural morphology. The following conservation equations are solved in the ECT coupled model:

Charge conservation in solid electrodes:

$$\nabla\cdot\left(\kappa_s^{eff}\nabla\phi_s\right)=j \tag{1}$$

Charge conservation in electrolyte:

$$\nabla\cdot\left(\kappa_e^{eff}\nabla\phi_e\right)+\nabla\cdot\left(\kappa_D^{eff}\nabla\ln c_e\right)=-j \tag{2}$$

Species conservation in electrolyte:

$$\frac{\partial(\varepsilon c_e)}{\partial t}=\nabla\cdot\left(D^{eff}\nabla c_e\right)+\frac{1-t_+}{F}j \tag{3}$$

Species conservation in active material particles:

$$\frac{\partial c_s}{\partial t}=\frac{1}{r^2}\frac{\partial}{\partial r}\left(D_s r^2\frac{\partial c_s}{\partial r}\right) \tag{4}$$

where κ, ϕ, c, D and j represent conductivity, electrical potential, concentration, diffusivity and volumetric current density respectively. The transport of lithium in the electrolyte and in the solid active materials are coupled by the following boundary condition applied at the particle surface:

$$-D_s\frac{\partial c_s}{\partial r}=\frac{j}{aF} \tag{5}$$

where a is the specific surface area of the electrode, and the volumetric current density j is calculated using the Butler-Volmer equation:

$$j=ai_0\left(\exp\left(\frac{\alpha_a F}{RT}\eta\right)-\exp\left(-\frac{\alpha_c F}{RT}\eta\right)\right) \tag{6}$$

Heat transfer is considered in this model to account for the effect of temperature on cell performance. The cell is treated as a single lumped unit, and its temperature is obtained via solving the following energy conservation equation:

$$mc_p\frac{\mathrm{d}T}{\mathrm{d}t}=Q+hA(T_\infty-T) \tag{7}$$

where Q is the heat generation power inside the cell, h the convective heat transfer coefficient, A the cell surface area, T the cell temperature and T_∞ the ambient temperature.

More detailed explanations for the above governing equations and associated boundary and initial conditions can be found in Ref. [31] and therefore are not repeated here. The design information of the LIB cell studied in this work is given in Table 1. Parameters related to the above equations, such as the properties of the graphite anode and the electrolyte, are taken either from the material database of Autolion™ [32,33], a commercial software package for analyses of electrochemical and thermal interactions of Li-ion batteries and systems, or from Ref. [31]. The properties of cathode materials, the $LiNi_{0.6}Co_{0.2}Mn_{0.2}O_2$, including the open-circuit potential, solid-state diffusivity and exchange current density, over a range of temperatures from −30 °C to 60 °C and electrolyte concentration from 0 to 4 M, are obtained from the experiments of Leng and Wang [34]. All the above governing equations are then solved via AutoLion™.

2.2. Diffusion-induced stress model

The DIS model is taken from the work of Cheng and Verbrugge [14], which is derived based on the analogy between DIS and thermal stress. Stress-driven diffusion, i.e. lithium diffusion under pressure gradient, is neglected in this model, which is reasonable given the much smaller time constant of lithium diffusion in graphite particle than that of mechanical deformation. With this assumption, the diffusion problem is completely decoupled from that of solid mechanics, enabling the calculation of radial and tangential stress in EAMPs using the concentration distribution of lithium obtained via solving Eq. (4). The radial and tangential stress along the particle radius are calculated as:

$$\sigma_r = \frac{2\Omega E}{3(1-\nu)}\left(\frac{1}{R^3}\int_0^R c_s r^2 dr - \frac{1}{r^3}\int_0^r c_s \xi^2 d\xi\right) \tag{8}$$

$$\sigma_\theta = \frac{\Omega E}{3(1-\nu)}\left(\frac{2}{R^3}\int_0^R c_s r^2 dr + \frac{1}{r^3}\int_0^r c_s \xi^2 d\xi - c_s\right) \tag{9}$$

where σ_r and σ_θ represent radial and tangential stress; Ω, E, and ν denote partial molar volume of lithium, Young's modulus and Possion's ratio; R is particle radius and r is coordinate along the radial direction; c_s is solid-phase lithium concentration at coordinate r, and ξ is the integration constant.

3. Results & discussion

3.1. Sinusoidal stress and current evolution

Fig. 1 presents the distributions of radial and tangential stresses within graphite particles at two different locations of the anode. One is close to the anode current-collecting foil (Fig. 1 a&c) and the other adjacent to the separator (Fig. 1 b&d). The cell is discharged in constant C-rate of 1C from 100% state of charge (SOC). Negative values in this figure represent compressive stress and positive values denote tensile stress. In consistence with the literature, the radial stress in graphite particles is compressive in discharge and highest in magnitude at the center of the particle. The tangential stress is compressive at the particle center and tensile at the surface. It is proposed by several authors [35,36] that the tensile tangential stress at particle surface is most detrimental to the cell durability, as there are numerous sub-micron cracks on the surface of graphite particles after electrode manufacturing process, and these surface cracks are prone to propagate under the tensile tangential stress. Our following discussion therefore will focus on the surface tangential stress (STS).

There are two interesting points regarding the stress distributions in Fig. 1. First, the STS of graphite at one specific position of the anode (i.e. stress value at x = 1.0 in either Fig. 1c or d) fluctuates with time in the discharge process. Second, if comparing the STS in Fig. 1c with that in Fig. 1d for same time instances, we can note that the STS is not always higher near the separator than that near the foil, as usually anticipated in the literature. In the reminder of the paper, we will focus on the temporal evolution behavior of STS in the discharge behavior and on the difference in these behaviors for graphite at different locations of the anode.

Fig. 2a presents the evolution of STS for graphite at different locations of the anode in the 1C discharge process. Each profile in this figure corresponds to one location in the anode, denoted by the dimensionless distance x which is defined as the ratio between the distance from the anode foil and the thickness of anode (x equals to zero for the anode/foil interface and to unity for the anode/separator interface). It is very interesting to note that the STS at all locations of the anode evolves like sinusoidal waves in the discharge process with several crests and troughs. The maximum value out of the entire discharge process for each profile in Fig. 2a is reached in the first crest. Also, the decline of STS near the separator is accompanied by the rise of STS near the foil, and vice versa. In certain period of time, the STS is even highest near the foil and lowest near the separator.

It can be drawn from Eq. (9) that the magnitude of STS is proportional to the difference between the average lithium concentration in the graphite particle and the concentration at the surface. Lithium concentration in the anode decreases in the discharge process, and the rate of concentration drop is affected by the discharge current. Fig. 2b presents the evolution of local transfer current in the 1C discharge process for graphite at different positions of the anode. The transfer current is plotted in terms of local C-rate, defined as the ratio between the current of selected mesh grid (integral of transfer current density over the volume of the grid) and the capacity of the corresponding mesh (overall cell capacity divided by the mesh number of anode). It can be seen from Fig. 2b that the evolution of local current is in very similar pattern with that of STS. The only difference is the time at which crests and troughs are reached. The concentration gradient inside the graphite particle, which governs the magnitude of STS, is proportional to the local transfer current density as can be seen from Eq. (5). It is therefore believed that the sinusoidal evolution of current is the

Table 1
Design parameters of the baseline cell.

Parameters	Anode (graphite)	Separator	Cathode (NCM622)
Thickness (μm)	48.7	25	40.75
Porosity	0.32	0.4	0.33
Loading (mAh/cm^2)	2.32	/	1.93
Electrolyte concentration (mol/L)	/	1.2	/
Particle radius (μm)	9	/	5

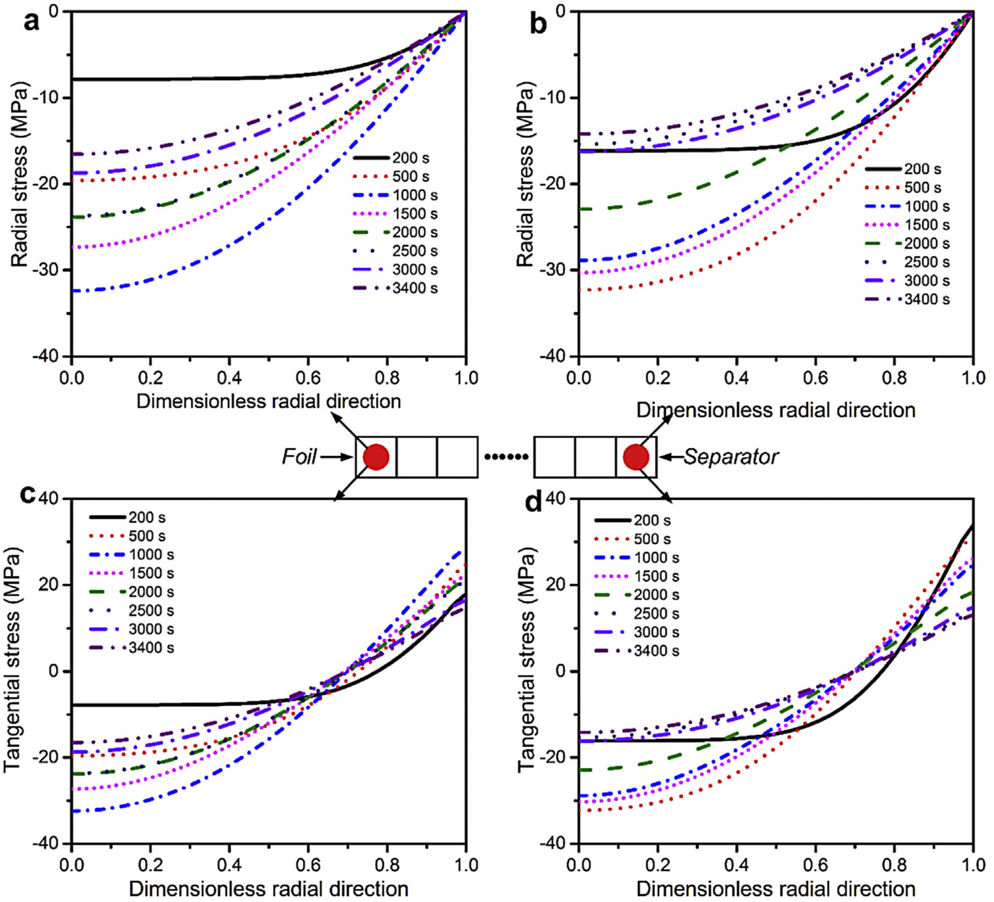

Fig. 1. Distributions of radial (a & b) and tangential (c & d) stresses along the radius of graphite particles at different times of the discharge process. The dimensionless radius is zero at the particle center and unity at the particle surface. The left two figures corresponds to graphite particles close to the anode foil, and the right two figures corresponds to graphite adjacent to the separator. The cell is discharged in constant C-rate of 1C from 100% state of charge.

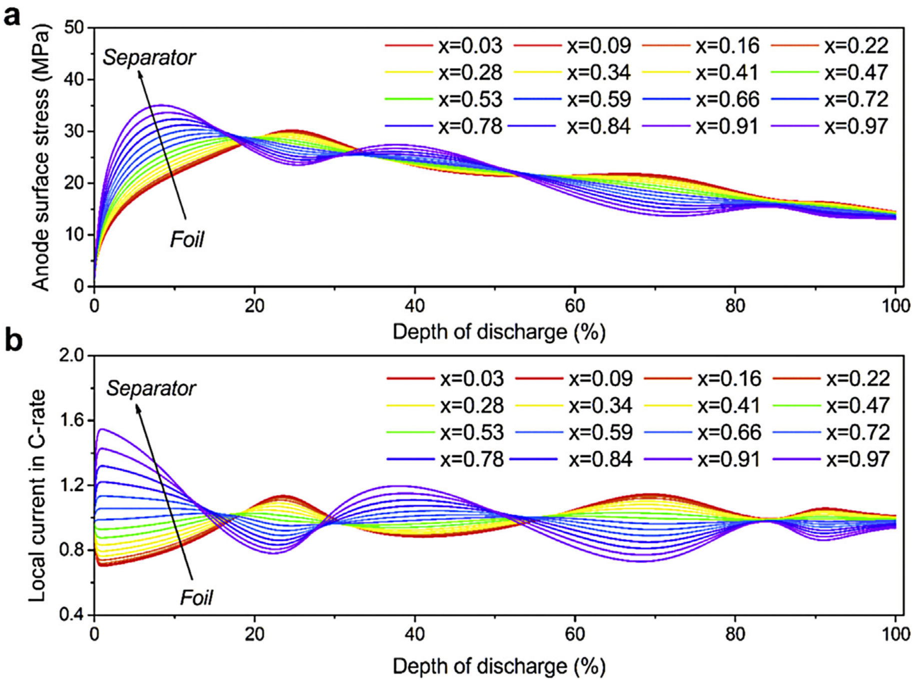

Fig. 2. Evolutions of (a) surface tangential stress and (b) local transfer current for graphite materials at different positions of the anode in the 1C discharge process from 100% state of charge. x represents dimensionless distance from the anode foil, which equals to zero at anode/foil interface and to unity at anode/separator interface.

reason why the STS evolves in a sinusoidal pattern. The diversity in time instances at which local current and STS reach crests and troughs is due to the fact that the buildup of concentration distribution within the graphite particle is slower in comparison to the changing rate of current, given the limited lithium diffusion capability inside the graphite particle.

Fig. 3a shows the evolution of local overpotential in the discharge process for different positions of the anode. The overpotential is the driving force for electrochemical reactions, and therefore its sinusoidal evolution, as presented in Fig. 3a, is the direct cause for the sinusoidal evolution of local transfer current. To demonstrate this more clearly, we plot in Fig. 4 the evolution of differential overpotential (the derivative of overpotential with respect to discharge capacity) for three selected locations of the anode. The profiles of local current at corresponding positions are also plotted for comparison. It is very interesting to note that the local current decreases when the differential overpotential is negative and increases when the differential overpotential is positive. We can also note that the time at which the differential overpotential reaches zero corresponds to the time at which the local current reaches its crest or trough.

The anode overpotential is defined as (ϕ_s-ϕ_e-$i\cdot R_{SEI}$-U_{ocp}), where ϕ_s and ϕ_e denote solid-phase and electrolyte-phase potentials; $i\cdot R_{SEI}$ is the ohmic drop across the SEI layer, and U_{ocp} *is* the open-circuit potential (OCP). The SEI resistance is negligible at room temperature; therefore the overpotential is governed by the difference between electrode potential (ϕ_s-ϕ_e, or -ϕ_e as $\phi_s \approx 0$ in the anode) and the OCP. In discharge, both electrode potential and OCP increase with time, but in different rates. The relative difference, i.e. the overpotential, therefore oscillates during discharge, as can be noted from the plot of differential overpotential in Fig. 4. Positive differential overpotential indicates faster rise of electrode potential over the rise of OCP, and vice versa. As mentioned above, local current density increases when the differential overpotential is positive, and decreases when the differential overpotential is negative. In other words, the local current increases when the OCP rise is slower, and decreases when OCP rise is faster. We shall note that the OCP of graphite is a function of lithium surface stoichiometry (LSS), as illustrated in Fig. A1 of Appendix, which has three plateaus (85 mV, 120 mV and 210 mV) corresponding to different stages of graphite [37]. The changing rate of OCP versus lithium stoichiometry is fairly small in the plateau regions, but large in the

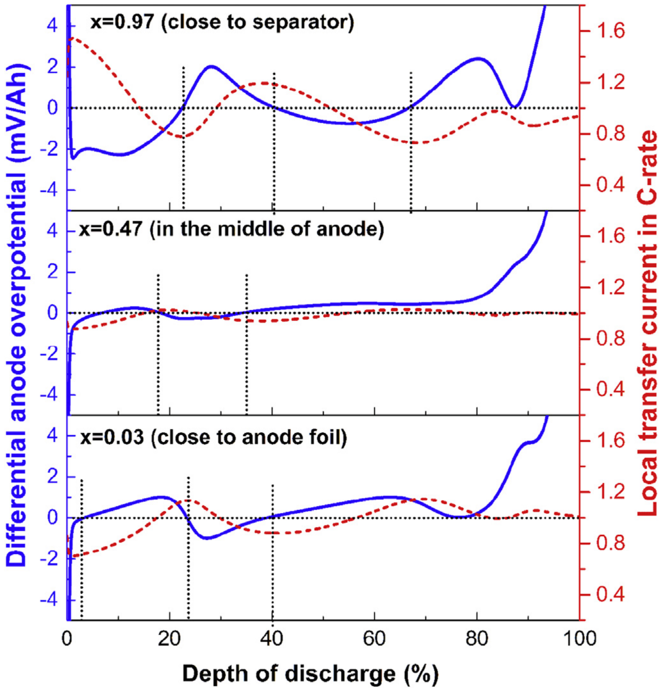

Fig. 4. Evolutions of differential overpotential (derivative of overpotential with respect to discharge capacity) and local transfer current in the 1C discharge process for graphite at three different positions of the anode.

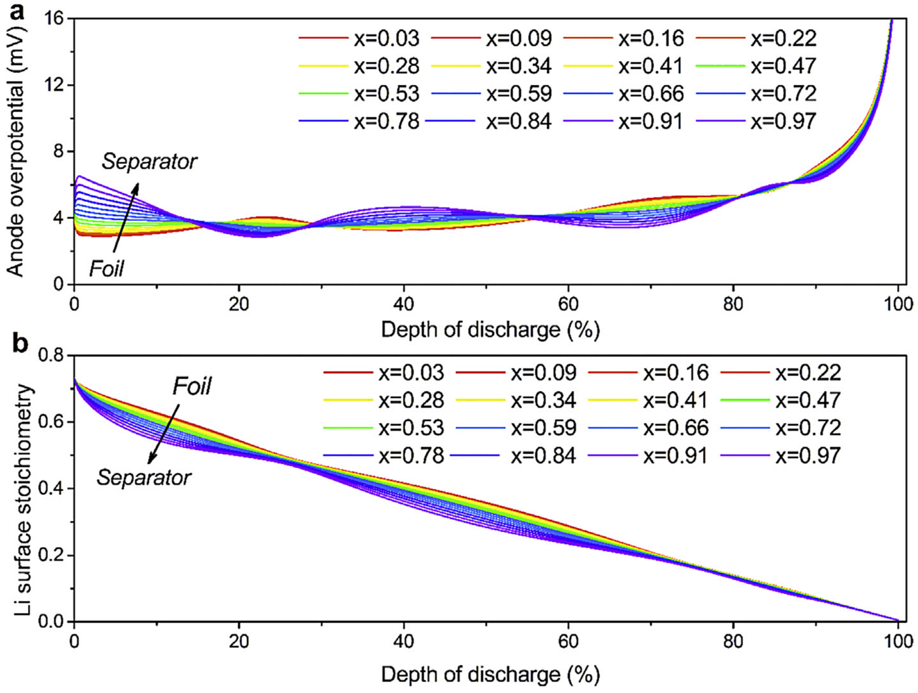

Fig. 3. Evolutions of (a) anode overpotential and (b) lithium surface stoichiometry for graphite materials at different positions of the anode in the 1C discharge process from 100% state of charge. x is dimensionless distance from the anode foil, which equals to zero at anode/foil interface and to unity at anode/separator interface.

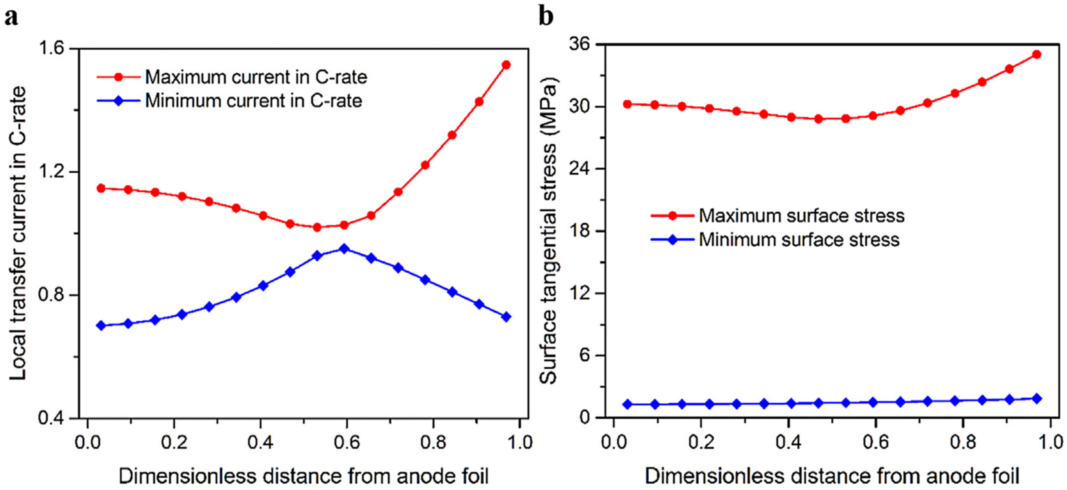

Fig. 5. Maximum and minimum (a) local transfer current in C-rate and (b) surface tangential stress in the discharge process for anode materials at different locations of the electrode.

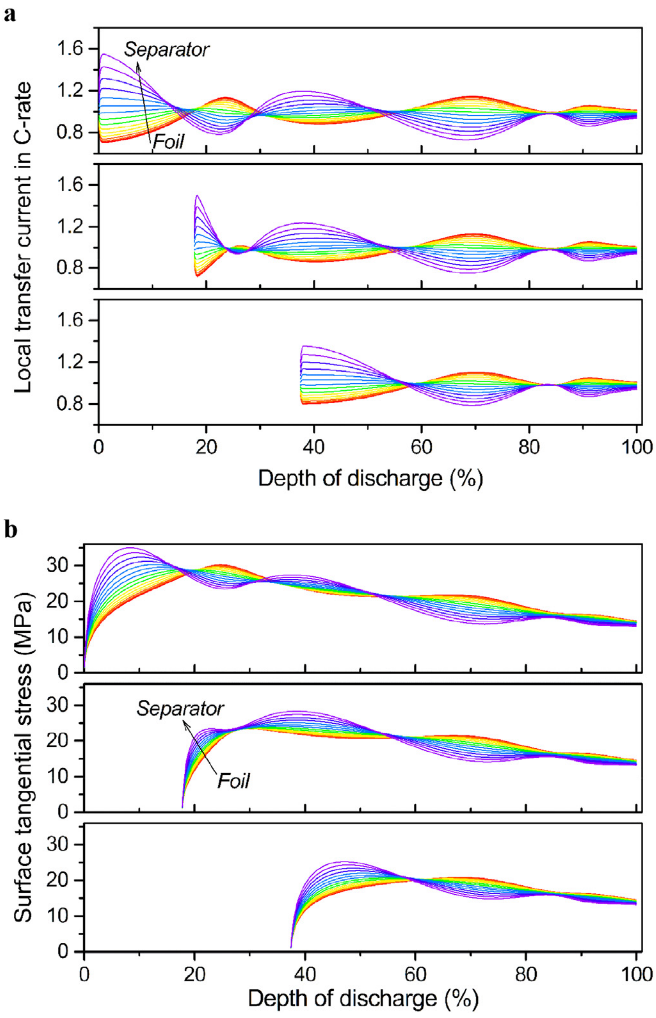

Fig. 6. Evolutions of (a) local transfer current in C-rate and (b) surface tangential stress for graphite at different locations of the anode in the 1C discharge process starting from different state of charges.

transition regions between two adjacent plateaus. Fig. 3b gives the evolution of LSS at different positions of the anode in the 1C discharge process. Due to the difference in local current density, the LSS at different locations of the anode drops at different rate with respect to discharge time. At one specific time instance, the LSS is highest near the foil and lowest near the separator, but it is interesting to note that the diversity of LSS across the anode expands and shrinks periodically in the discharge process. Moreover, it should be stressed that the LSSs around which all profiles in Fig. 3b converge precisely coincide with the stoichiometry points at which the OCP of graphite transit from one plateau to another (referring to Fig. A1). In other words, the discharge process in Fig. 3b can be divided into three parts. The first part is from the beginning of discharge to 25% depth of discharge (DoD), which corresponds to stage-I of graphite in its OCP curve (the 85 mV plateau in Fig. A1). The second part is from 25% DoD to 70% DoD, corresponding to the 120 mV plateau of graphite OCP. The reminder is the third part. In each of the three parts, the LSS gradient across the anode increases at the beginning and shrinks in the end. Comparing the profiles in Figs. 2 and 3a with Fig. 3b, we can also note that the evolution profiles of STS, local current and anode overpotential undergo one crest and one trough in each of the three parts. If treating these evolution profiles as sinusoidal waves, the period of these sine waves corresponds to the duration of graphite staying in each of its stages.

The relationship between the staging behavior of graphite and the sinusoidal patterns of current and stress evolutions are attributed to different changing rate of OCV with respect to LSS at different LSSs along with the diversity of LSS across the anode. Before discharge, LSS is uniform across the entire anode. The local current is therefore highest near the separator at the beginning of discharge due to the lowest ionic resistance there. The higher local current leads to faster drop of LSS and accordingly faster rise of OCP near the separator, especially when approaching the transition region in between two OCP plateaus. The faster rise of OCP near the separator results in faster drop of anode overpotential and therefore in reduction of local current therein. Since the overall output current is constant, the local current in other part of the anode, e.g. the region near the anode foil, starts to increase. In accordance with the drop of current near the separator and rise of current near the foil, the decrease of LSS slows down near the separator and speeds up near the foil, making the LSSs at different locations move closer to each other. Once the OCP of graphite near the separator enters another plateau region, the rate of OCP rise slows down, and the overpotential therefore starts bouncing back, leading to rise of local

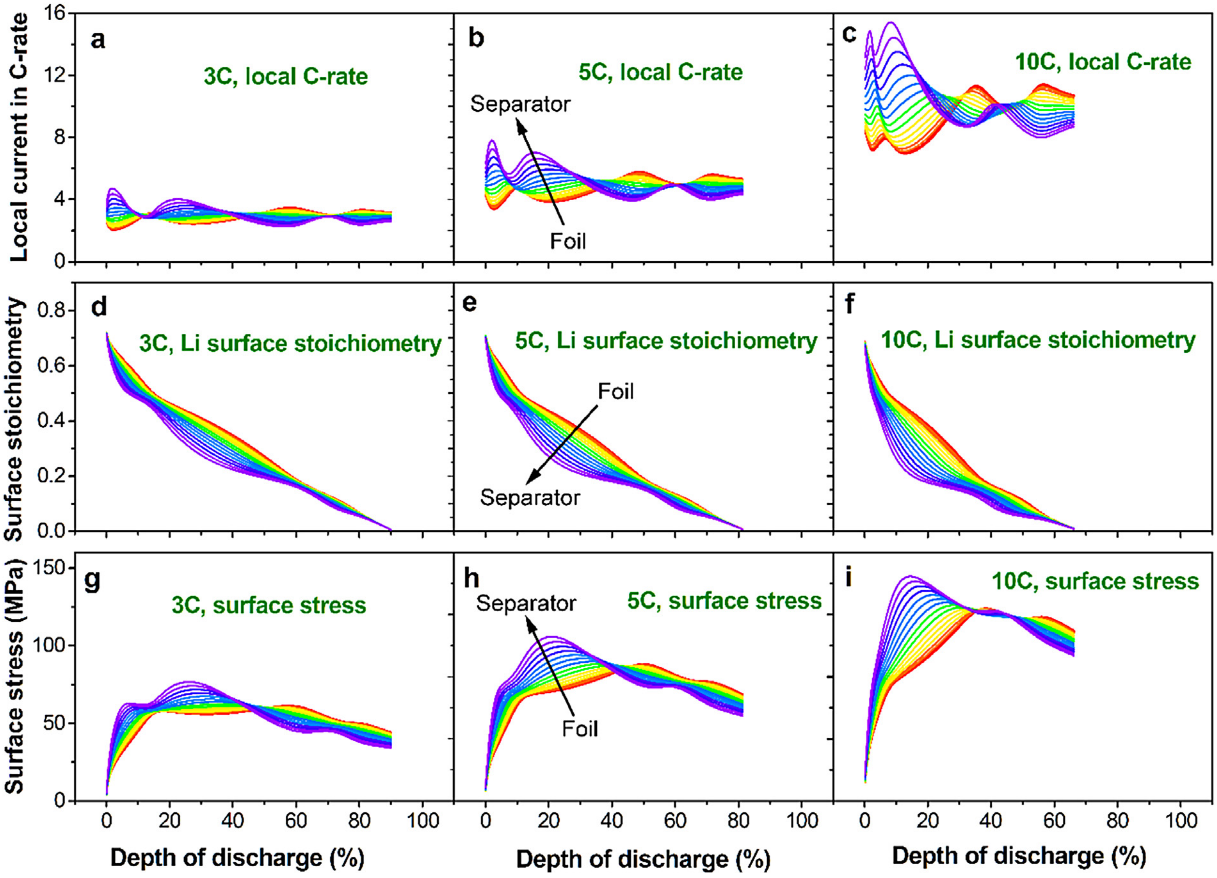

Fig. 7. Evolutions of (a–c) local transfer current in C-rate (d–f) lithium surface stoichiometry and (g–i) surface tangential stress for graphite at different locations of the anode in the discharge process at different C-rates.

current. In the meantime, the OCP of graphite near the foil is still in the transition region with faster increase of OCP and therefore faster drop of overpotential. As a consequence, the local current near the foil begin to decrease.

To sum up, the staging behavior of graphite, especially the sharp change of OCP in the region between two plateaus, acts as barriers to further divergence of LSS across the anode and therefore balances the current generation at different positions of the anode. It should be mentioned that some of most recent experimental studies [38–40] observed certain similarity between the differential cell strains and differential cell voltage (i.e. $d\varepsilon/dQ$ similar to dV/dQ). The sinusoidal evolution pattern of STS and its correlation with the staging behavior of graphite could be potential reasons for these experimental findings.

It should be mentioned that the sinusoidal current and STS evolutions result in different ranges of local current and STS in the entire discharge process for graphite materials at different positions of the anode, as can be seen from Fig. 5 where the maximum and minimum local transfer current and STS out of the entire 1C discharge process are plotted for graphite at different positions in the anode. We can observe that the region close to the separator has the highest range of current and STS variation in the discharge process. Moreover, it is interesting to note that the smallest range of current and STS variation occurs not in the region close to the anode foil, but in the region near the middle of anode thickness.

3.2. *Effect of starting state of charge*

From the above analysis we can learn that the evolution of current and STS is affected by the staging behavior of graphite. The maximum current and STS out of the entire discharge process occur in the first crest of the corresponding evolution profiles, which is in stage-I of graphite (referring to Fig. A1) if discharging from 100% SOC. In solid mechanics it is believed that the crack propagation rate is mostly affected by the maximum stress in each cycle (e.g. the Paris law). From the viewpoint of alleviating mechanical degradation, it is therefore important to reduce the maximum STS in the discharge process. It is proposed in the literature [41] that the starting SOC of discharge has great impact on the delamination onset of electrode materials. Here in this section, the effect of starting SOC on the maximum STS is investigated, as shown in Fig. 6 where the evolutions of local current and STS for cases discharging from different SOCs are presented. For all cases studied, the local current and STS evolve in similar sinusoidal patterns as these evolutions are related to the staging behavior of graphite. Nevertheless, it is clearly demonstrated that the maximum local current and STS are reduced with the decrease of starting SOC. Therefore, operating the battery in low SOC window can be beneficial to the cell durability.

3.3. *Effect of C-rate*

The effects of discharge C-rate on the evolutions of current and STS are investigated by discharging the cell in various C-rate (3C, 5C and 10C) from 100% SOC. The corresponding evolutions of local transfer current, LSS and STS for graphite at different positions of the anode are plotted in Fig. 7. As shown in this figure, the increase of overall discharge rate leads to much larger differences in C-rate

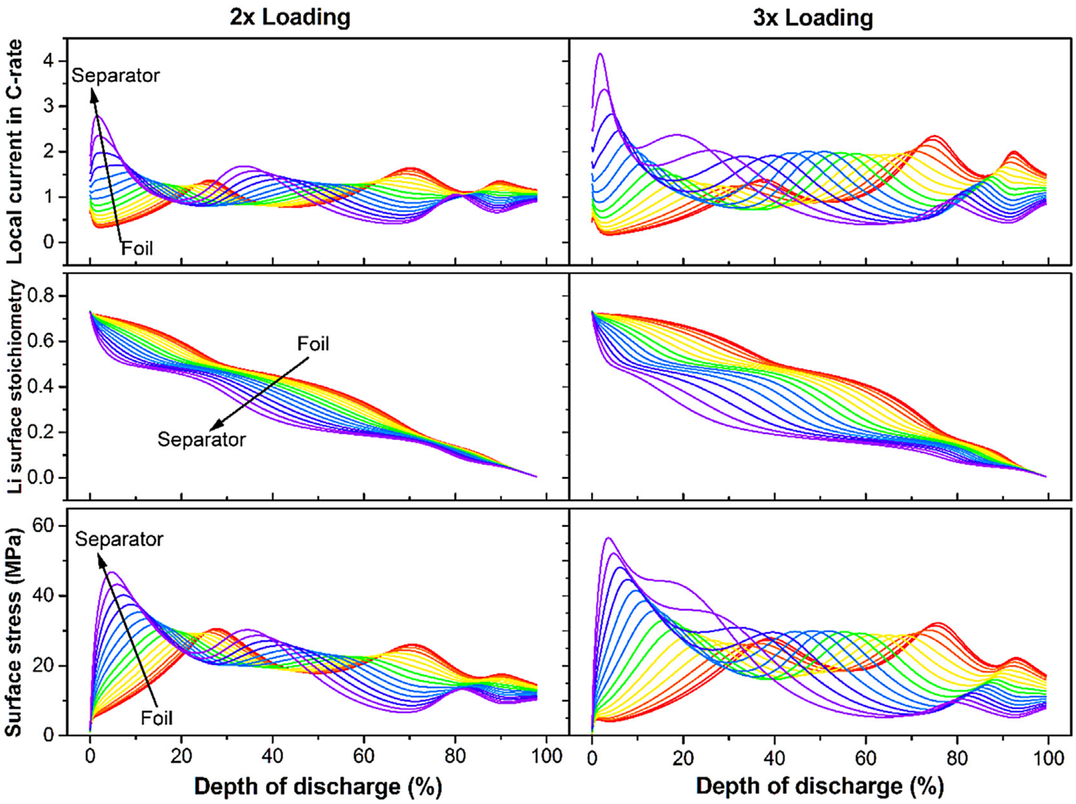

Fig. 8. Evolution of local current in C-rate, lithium surface stoichiometry and surface tangential stress in the discharge process for cells with different energy densities. The left three figures have 2× thickness and areal loading of active materials in comparison to the base case cell, and the right three figures have 3× electrode thickness and areal loading. Both cells are discharged from 100% state of charge in 1C.

across the electrode, as shown in Fig. 7a–c. As a consequence, the LSS gradient across the anode becomes much larger with increased C-rate. The convergence of LSS profiles around the stage transition region of graphite, as noted in Fig. 3b for 1C discharge, becomes less apparent or even disappears with the increase of discharge rate, as can be seen from Fig. 7d–f. In addition, the magnitude of STS also increases with the increase of C-rate. It should be mentioned that the maximum STS of the discharge process in high C-rate is reached not in the first crest (stage-I of graphite) of its evolution profile as in the 1C discharge, but in the second crest (stage-II of graphite). This can be attributed to the slower diffusion process of lithium inside the graphite particle in comparison with the fast drop of LSS at high C-rate, which delayed the occurrence of maximum difference between surface and average lithium concentrations.

3.4. *Effect of electrode thickness*

We further investigated the effects of electrode thickness on the current and stress evolutions. The advancement of EVs require the LIBs to have high energy density. One practical approach to increase energy density is to increase the loading of active materials. In this section two cells with higher energy densities than the base-case cell presented above are studied. One has double electrode thickness and double areal loading of the base-case cell, and the other has triple electrode thickness and triple areal loading. Both cells are discharged in 1C from 100% SOC. The evolutions of local transfer current, LSS and STS for graphite at different anode locations are presented in Fig. 8 for the two high-energy cells. Comparing the evolution profiles in Fig. 8 with those in Figs. 2 and 3 of the base case, we can learn that the increase of electrode thickness leads to more non-uniform current and stress distributions. Though the overall discharge rate is 1C, the maximum local C-rate is as high as 3C for the 2x-loading cell and 4C for the 3x-loading cell, much larger than the base-case cell in which the maximum local C-rate is only 1.6C. The increase of electrode thickness also leads to much larger LSS gradient across the anode. Furthermore, the magnitude of STS also increases with higher electrode thickness, especially in the region close to the separator. It can be concluded that the high energy cells with high electrode thickness are more prone to mechanical degradation due to the high DIS.

4. Conclusion

A single-particle DIS model is incorporated into an ECT coupled model to predict the stress distribution across the electrode thickness in the discharge process of LIBs. Special attention is paid to the evolution of stress, as well as local current, in the entire discharge process for graphite materials at different positions of the anode. We found that the local current and STS evolve like decaying sinusoidal waves in the discharge process, with several crests and troughs. The staging behavior of graphite, in particular the sharp variation of graphite OCP in between two plateaus, is found to be the root cause for the sinusoidal patterns of current and stress evolutions. At low discharge rate, the maximum STS of the entire discharge process for each position of the anode occurs in the first stage of graphite. Reducing the maximum SOC in battery operation can alleviate the maximum STS and therefore be helpful for cell durability. With the increase of discharge rate, the current and stress distributions in the anode become much more non-uniform, and the maximum STS of the discharge process is postponed to the second stage of graphite with much larger values. Furthermore, high-energy cells with higher electrode thickness have much more non-uniform current and stress distributions, and are more prone to mechanical degradation due to much higher DIS.

Acknowledgements

We greatly acknowledge BMW for financial support of this work, EC Power for donating AutoLion™ software licenses to support this research, and Umicore for cathode material support.

Appendix A. Supplementary data

Supplementary data related to this article can be found at http://dx.doi.org/10.1016/j.jpowsour.2016.07.070.

Nomenclature

A	cell surface area, m^{2}
c	lithium concentration, mol m^{-3}
D	Diffusion coefficient, m^{2} s^{-1}
E	Young's modulus, Pa
F	Faraday constant, 96487 C mol^{-1}
h	heat transfer coefficient, W m^{-2}K^{-1}
j	volumetric current density, A m^{-3}
m	cell mass, kg
Q	heat source, W
R	particle radius, m
t	time, s
t_+	transference number
T	temperature, K

Greek

ε	porosity
κ	conductivity, S m^{-1}
κ_D	diffusional conductivity, A m^{-1}
Ω	Partial molar volume, m^{3} mol^{-1}
σ	stress, Pa
ϕ	electric potential, V
ν	Possion's ratio

Subscripts

e	electrolyte phase
r	radial direction
s	solid phase
θ	tangential direction

Superscripts

eff	effective

References

[1] M.R. Palacín, A. de Guibert, Science 351 (2016) 1253292.

[2] V. Etacheri, R. Marom, R. Elazari, G. Salitra, D. Aurbach, Energy Environ. Sci. 4 (2011) 3243–3262.

[3] J. Vetter, P. Novák, M.R. Wagner, C. Veit, K.C. Möller, J.O. Besenhard, M. Winter, M. Wohlfahrt-Mehrens, C. Vogler, A. Hammouche, J. Power Sources 147 (2005) 269–281.

[4] M. Broussely, P. Biensan, F. Bonhomme, P. Blanchard, S. Herreyre, K. Nechev, R.J. Staniewicz, J. Power Sources 146 (2005) 90–96.

[5] A. Barré, B. Deguilhem, S. Grolleau, M. Gérard, F. Suard, D. Riu, J. Power Sources 241 (2013) 680–689.

[6] W.H. Woodford, Y.-M. Chiang, W.C. Carter, J. Electrochem. Soc. 157 (2010) A1052–A1059.

[7] P. Liu, J. Wang, J. Hicks-Garner, E. Sherman, S. Soukiazian, M. Verbrugge, H. Tataria, J. Musser, P. Finamore, J. Electrochem. Soc. 157 (2010) A499–A507.

[8] K. Zhao, M. Pharr, J.J. Vlassak, Z. Suo, J. Appl. Phys. 108 (2010) 073517.

[9] R. Kostecki, F. McLarnon, J. Power Sources 119–121 (2003) 550–554.

[10] J. Christensen, J. Newman, J. Electrochem. Soc. 153 (2006) A1019–A1030.

[11] J. Christensen, J. Newman, J. Solid State Electrochem. 10 (2006) 293–319.

[12] X. Zhang, W. Shyy, A. Marie Sastry, J. Electrochem. Soc. 154 (2007) A910–A916.

[13] X. Zhang, A.M. Sastry, W. Shyy, J. Electrochem. Soc. 155 (2008) A542–A552.

[14] Y.T. Cheng, M.W. Verbrugge, J. Power Sources 190 (2009) 453–460.

[15] M.W. Verbrugge, Y.-T. Cheng, J. Electrochem. Soc. 156 (2009) A927–A937.

[16] Y.T. Cheng, M.W. Verbrugge, J. Electrochem. Soc. 157 (2010) A508–A516.

[17] B. Suthar, V. Ramadesigan, S. De, R.D. Braatz, V.R. Subramanian, Phys. Chem. Chem. Phys. 16 (2014) 277–287.

[18] R.E. Garcıa, Y.-M. Chiang, W. Craig Carter, P. Limthongkul, C.M. Bishop, J. Electrochem. Soc. 152 (2005) A255–A263.

[19] M. Doyle, T.F. Fuller, J. Newman, J. Electrochem. Soc. 140 (1993) 1526–1533.

[20] T.F. Fuller, M. Doyle, J. Newman, J. Electrochem. Soc. 141 (1994) 1–10.

[21] J. Christensen, J. Electrochem. Soc. 157 (2010) A366–A380.

[22] S. Golmon, K. Maute, M.L. Dunn, Comput. Struct. 87 (2009) 1567–1579.

[23] S. Renganathan, G. Sikha, S. Santhanagopalan, R.E. White, J. Electrochem. Soc. 157 (2010) A155–A163.

[24] Y. Dai, L. Cai, R.E. White, J. Power Sources 247 (2014) 365–376.

[25] K. Takahashi, V. Srinivasan, J. Electrochem. Soc. 162 (2015) A635–A645.

[26] B. Suthar, P.W.C. Northrop, D. Rife, V.R. Subramanian, J. Electrochem. Soc. 162 (2015) A1708–A1717.

[27] W.B. Gu, C.Y. Wang, J. Electrochem. Soc. 147 (2000) 2910–2922.

[28] V. Srinivasan, C.Y. Wang, J. Electrochem. Soc. 150 (2003) A98–A106.

[29] K. Smith, C.Y. Wang, J. Power Sources 160 (2006) 662–673.

[30] W. Fang, O.J. Kwon, C.Y. Wang, Int. J. Energy Res. 34 (2010) 107–115.

[31] Y. Ji, Y. Zhang, C.Y. Wang, J. Electrochem. Soc. 160 (2013) A636–A649.

[32] AutoLion^{TM}, www.ecpowergroup.com/autolion/.

[33] J. Kalupson, G. Luo, C.E. Shaffer, SAE Technical Paper, (2013) 01–1522.

[34] Y. Leng, C.Y. Wang, Unpublished Research, Penn State University Electrochemical Engine Center, University Park, PA, 2015, 16802.

[35] R. Deshpande, M. Verbrugge, Y.-T. Cheng, J. Wang, P. Liu, J. Electrochem. Soc. 159 (2012) A1730–A1738.

[36] J. Purewal, J. Wang, J. Graetz, S. Soukiazian, H. Tataria, M.W. Verbrugge, J. Power Sources 272 (2014) 1154–1161.

[37] T. Ohzuku, Y. Iwakoshi, K. Sawai, J. Electrochem. Soc. 140 (1993) 2490–2498.

[38] K.Y. Oh, J.B. Siegel, L. Secondo, S.U. Kim, N.A. Samad, J. Qin, D. Anderson, K. Garikipati, A. Knobloch, B.I. Epureanu, C.W. Monroe, A. Stefanopoulou, J. Power Sources 267 (2014) 197–202.

[39] L.W. Sommer, A. Raghavan, P. Kiesel, B. Saha, J. Schwartz, A. Lochbaum, A. Ganguli, C.J. Bae, M. Alamgir, J. Electrochem. Soc. 162 (2015) A2664–A2669.

[40] Z.J. Schiffer, J. Cannarella, C.B. Arnold, J. Electrochem. Soc. 163 (2015) A427–A433.

[41] B. Lu, Y. Song, J. Zhang, J. Power Sources 289 (2015) 168–183.